Flow past an impulsively started circular cylinder using a higher-order semicompact scheme

Y. V. S. S. Sanyasiraju* and V. Manjula
Department of Mathematics, Indian Institute of Technology Madras, Chennai-600036, India
(Received 26 October 2004; published 18 July 2005)

In the present investigation an attempt has been made to solve the two-dimensional incompressible viscous flow past an impulsively started circular cylinder for Reynolds numbers ranging from 20 to 5000 using higher-order semicompact scheme (HOSC). Unlike conventional higher-order compact schemes the HOSC scheme has been developed to handle the circular geometry of the chosen problem and the intensive algebraic manipulations have been reduced considerably by relaxing the compactness of the computational stencil for few terms (but retained for most of the terms) of the discretized equations. For the flow past an impulsively started circular cylinder the results obtained at low and moderate Reynolds numbers have been validated with the experimental and numerical observations available in the literature. For high Reynolds number flows, the present scheme rightly captures the α phenomenon at Re=1000 and both β and α phenomena one after the other at Re=5000.

DOI: 10.1103/PhysRevE.72.016709 PACS number(s): 47.11.+j, 02.70.−c, 95.75.Pq, 83.85.Pt

I. INTRODUCTION

The classical problem of viscous incompressible flow past an impulsively started circular cylinder, which is being used as a prototype of unsteady separated flows has been the subject of many experimental, theoretical, and computational investigations for the past several decades. Although the geometry is simple, the flow phenomenon is complex especially for large Reynolds numbers. Therefore, obtaining solutions to the governing Navier-Stokes equations is very challenging and has generated considerable interest to find the analytical solutions [1–8]. In these investigations the flow for times after the start is considered using the boundary layer theory. The basis of these applications of unsteady boundary layer theory is to expand the flow variables in powers of the time from the start of the position and they are necessarily limited to small times after the start. However, the results fortunately indicated the basic structure of the initial position. There are also many experimental investigations on unsteady flow past an impulsively started circular cylinder [9–12]. Among them [12] is the latest and the development of the main and secondary vortices has been studied qualitatively and quantitatively in detail for Reynolds numbers up to 10^4. Indeed it is in this study that the presence of secondary eddy phenomenon which has a rotation opposite to that of the main eddy due to second separation of the flow was reported experimentally. On the other hand, there is another category of purely numerical schemes to solve Navier-Stokes equations initiated by [13] for Re=40 and 100 (here $\mathrm{Re}=Ud/\nu$ where d is the diameter of the cylinder, U is the characteristic velocity, and ν is the coefficient of kinematic viscosity). The same problem has also been considered by [14–19] for Reynolds numbers ranging from 10 to 500. The major interest in these investigations is the development of the unsteady separated wake behind the cylinder as a function of time and its structure for large values of the time. Based on the existing results, the flow patterns can be divided into three categories depending on the value of the Reynolds number. The flows with Reynolds number less or equal to 60 comes in the first category wherein the unsteady flow computations can be made until steady state. The flow in this range of Reynolds number remains symmetric with respect to the x axis. Therefore, the half domain with positive y is sufficient for obtaining the numerical solutions. The second category ranges the Reynolds number from 60 to 800 wherein the flow is symmetric for small time steps. Reference [12] observed formation of bulge and secondary eddy phenomena at time 2.5 in this range of Re and demonstrated the same at Reynolds numbers 300 and 550, respectively. Due to the onset of the asymmetry at large times, computations in this range of Reynolds number have to be carried out around the full circle. However, if the aim is to understand the flow phenomena at the beginning of the translation, then the computations can still be carried out on one half of the domain. The third category can be taken for high Reynolds numbers where the interest is focussed close to the cylinder and early time steps. At these Reynolds numbers, [12] showed the development of two interesting flow phenomena called phenomenon α for Re greater than 800 and phenomenon β for Re 5000 and above. To establish numerically these complex flow phenomena for flow past an impulsively started circular cylinder, the investigators until now have used Re=3000 to demonstrate α phenomenon and Re =9500 for β phenomenon. Though it is known experimentally that both these phenomena must occur one after the other at Re=5000, so far there has not been any evidence of such numerical simulation having been reported.

For the past few years, application of higher-order compact (HOC) schemes to viscous incompressible flow calculations has been attracting many researchers due to their higher degree of accuracy and smaller stencil. References [20–23] are some of the early investigators who have developed fourth-order schemes to stream function-vorticity equations on compact molecules. All these investigations are centered on steady flows and the developed schemes have been tested for lid driven cavity problem in square domains. Reference

*Electronic address: sryedida@iitm.ac.in

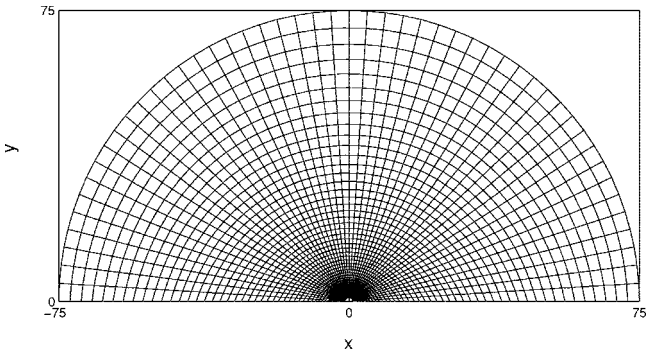

FIG. 1. Computational mesh.

[24] has developed and applied several higher-order schemes for time dependent diffusion and convection-diffusion problems and [25] used the HOC approach in the transient Euler equations in one- and two-dimensional problems. Reference [26] also proposed a scheme for time dependent problems similar to the scheme proposed by them for the steady case. These investigations show that there is some attempt to realize the solutions of time dependent diffusion and convection-diffusion problems using HOC schemes. Reference [27] developed an essentially compact scheme by simplifying the algebraic manipulations involved for the Navier-Stokes equations in stream function vorticity formulation. Reference [28] developed a higher-order semicompact (HOSC) scheme in the lines of essentially compact scheme to the unsteady flows in curved geometries. In the HOSC scheme the algebraic manipulations have been simplified by sacrificing compactness of the numerical scheme for certain terms of the governing equations. The main advantage of the semicompact scheme is that at any time level there are only two elliptic types of equations to be solved, one each for stream function and vorticity along with a parabolic equation for time marching.

The purpose of the present investigation is to test the HOSC scheme to solve a problem with complex flow phenomenon in nonrectangular geometry. To the best of our knowledge no work has been reported until now applying the compact schemes to flow problems in nonrectangular domains except [29–31], who developed compact fourth-order schemes to linear Poisson or quasilinear Poisson equations in polar coordinates. However these investigations are limited to the Poisson-type equations. If the domain of interest is nonrectangular, the finite difference methodology of higher-order compact schemes further complicates the already very complicated algebraic manipulations. Therefore, in the present work we have used the higher-order semicompact scheme to solve flow past an impulsively started circular cylinder in curvilinear coordinate system. The curvilinear system is generated by solving elliptic partial differential equations of a body fitted coordinate system proposed by [32].

II. MATHEMATICAL FORMULATION

A. Governing equations

Consider the two-dimensional unsteady incompressible Navier-Stokes equations in stream function vorticity form in Cartesian coordinates

$$\frac{\partial^2\psi}{\partial x^2}+\frac{\partial^2\psi}{\partial y^2}=-\omega, \tag{1}$$

$$\frac{\partial\omega}{\partial t}+u\frac{\partial\omega}{\partial x}+v\frac{\partial\omega}{\partial y}=\frac{1}{\mathrm{Re}}\left(\frac{\partial^2\omega}{\partial x^2}+\frac{\partial^2\omega}{\partial y^2}\right), \tag{2}$$

where ψ is the stream function defined by $u=\partial\psi/\partial y$, $v=-\partial\psi/\partial x$ and ω is the vorticity defined by $\omega=v_x-u_y$, and u and v are components of the velocity in x and y directions, respectively.

To accommodate the computations on an arbitrary geometry, the Cartesian coordinates are transformed into curvilinear coordinates (ξ,η) using body fitted coordinates given by [32]. The governing equations in the computational coordinates (ξ,η) are

$$\frac{1}{J^2}\left(\alpha\frac{\partial^2\psi}{\partial\xi^2}-2\beta\frac{\partial^2\psi}{\partial\xi\,\partial\eta}+\gamma\frac{\partial^2\psi}{\partial\eta^2}\right)=-\omega, \tag{3}$$

$$\frac{\partial\omega}{\partial t}=-\frac{1}{J}\left(\frac{\partial\psi}{\partial\eta}\frac{\partial\omega}{\partial\xi}-\frac{\partial\psi}{\partial\xi}\frac{\partial\omega}{\partial\eta}\right)+\frac{1}{\mathrm{Re}}\frac{1}{J^2}\left(\alpha\frac{\partial^2\omega}{\partial\xi^2}-2\beta\frac{\partial^2\omega}{\partial\xi\,\partial\eta}+\gamma\frac{\partial^2\omega}{\partial\eta^2}\right), \tag{4}$$

$$u=\frac{1}{J}\left(\frac{\partial x}{\partial\xi}\frac{\partial\psi}{\partial\eta}-\frac{\partial x}{\partial\eta}\frac{\partial\psi}{\partial\xi}\right),\quad v=-\frac{1}{J}\left(\frac{\partial y}{\partial\eta}\frac{\partial\psi}{\partial\xi}-\frac{\partial y}{\partial\xi}\frac{\partial\psi}{\partial\eta}\right), \tag{5}$$

$$\text{where } \alpha=\left(\frac{\partial x}{\partial\eta}\right)^2+\left(\frac{\partial y}{\partial\eta}\right)^2,\quad \beta=\left(\frac{\partial x}{\partial\xi}\right)\left(\frac{\partial x}{\partial\eta}\right)+\left(\frac{\partial y}{\partial\xi}\right)\left(\frac{\partial y}{\partial\eta}\right),\quad \gamma=\left(\frac{\partial x}{\partial\xi}\right)^2+\left(\frac{\partial y}{\partial\xi}\right)^2, \tag{6}$$

TABLE I. Effect of far field boundary on wake length and separation angle.

	Re=20			Re=40		
D	50.5	62.5	75	50.5	62.5	75
θ_s	41.9518	41.4694	41.3277	51.8720	51.1700	51.0249
L	1.759841	1.760388	1.773829	4.130092	4.205498	4.210746

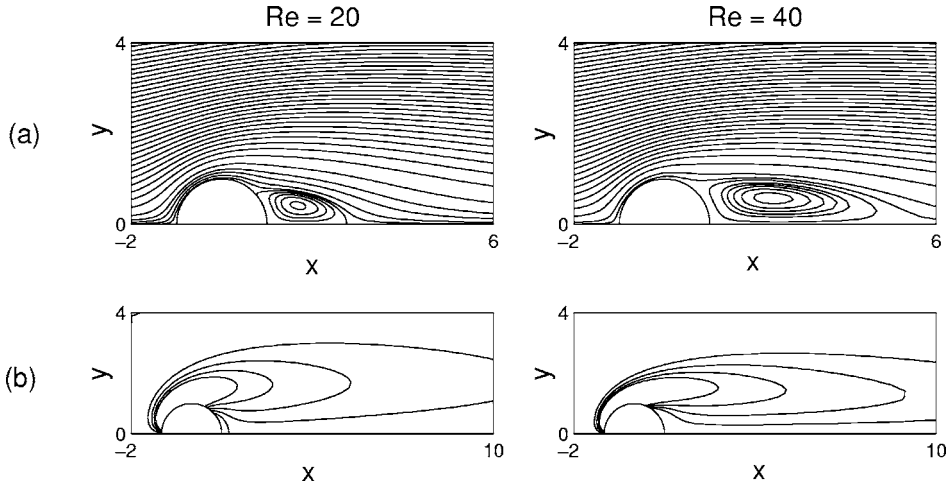

FIG. 2. (a) Stream lines and (b) vorticity contours at Re=20 and 40.

$$\text{and} \quad J = \left(\frac{\partial x}{\partial \xi}\right)\left(\frac{\partial y}{\partial \eta}\right) - \left(\frac{\partial x}{\partial \eta}\right)\left(\frac{\partial y}{\partial \xi}\right). \tag{6a}$$

α, β, γ, and J depend on the geometry and hence calculated only once in the entire iterative process and stored once for all. Since the problem under investigation has cylindrical geometry, the geometric parameters in Eq. (6) can be computed exactly. However, to verify the influence of these terms on the accuracy of the final results, the terms in Eq. (6) have been computed using exact functions and also using numerical approximations. The numerical approximation of Eq. (6) is required due to the nonavailability of the exact computation of terms in Eq. (6) for the problems on irregular geometries. It is found that the difference between these computations is marginal and hence all the computations for high Reynolds numbers have been carried out using numerical approximations of Eq. (6). Finally, Eqs. (3) and (4) have to be solved on the rectangular computational domain (ξ, η).

III. HIGHER-ORDER SEMICOMPACT SCHEME

A. Discretization

The complete details of the higher-order semicompact space discretization of Eqs. (3) and (4) have been given in [28] and their final form is given by

$$\mathsf{F}(\psi) = -J^2\bar{\omega} + O(h^4), \tag{7}$$

$$\frac{\partial \bar{\omega}}{\partial t} = \frac{1}{J^2}\frac{1}{\mathrm{Re}}\mathsf{F}(\omega) + \frac{h^2}{12}(D_\xi^3\psi D_\eta\omega - D_\eta^3\psi D_\xi\omega - D_\eta\psi D_\xi^3\omega + D_\xi\psi D_\eta^3\omega) - D_\eta\psi D_\xi\omega - D_\xi\psi D_\eta\omega + \frac{h^2}{12}(D_\xi^2 D_\eta\psi D_\xi\omega + D_\eta\psi D_\eta^2 D_\xi\omega - D_\eta^2 D_\xi\psi D_\eta\omega - D_\xi\psi D_\xi^2 D_\eta\omega) + O(h^4), \tag{8}$$

$$\mathsf{F} = \left\{\alpha D_\xi^2\left(1 + \frac{h^2}{12}D_\eta^2\right) - 2\beta D_\xi D_\eta\left(1 - \frac{h^2}{12}(D_\xi^2 + D_\eta^2)\right) + \gamma D_\eta^2\left(1 + \frac{h^2}{12}D_\xi^2\right)\right\}, \tag{9}$$

where

$$\bar{\omega} = \left(1 + \frac{h^2}{12}(D_\xi^2 + D_\eta^2)\right)\omega, \tag{10}$$

$$D_\xi f(\xi,\eta) = \frac{f(\xi+h,\eta) - f(\xi-h,\eta)}{2h}, \tag{11}$$

$$D_\eta f(\xi,\eta) = \frac{f(\xi,\eta+h) - f(\xi,\eta-h)}{2h}, \tag{12}$$

$$D_\xi^2 f(\xi,\eta) = \frac{f(\xi+h,\eta) - 2f(\xi,\eta) + f(\xi-h,\eta)}{h^2}, \tag{13}$$

$$D_\eta^2 f(\xi,\eta) = \frac{f(\xi,\eta+h) - 2f(\xi,\eta) + f(\xi,\eta-h)}{h^2}. \tag{14}$$

α, β, and γ are computed from the geometry transformation and hence treated as constants. The third-order difference terms in Eqs. (7)–(9) are the ones which make the present scheme semicompact. All other terms in these equations are approximated to fourth order on a compact molecule. Further, the way the boundary conditions are applied at the artificial cut of the body fitted coordinate system and far field, it is only at the neighborhood of the surface of the cylinder that the present scheme requires one sided differences (only for vorticity) for the third-order terms in Eqs. (7)–(9).

TABLE II. Effect of grid size on wake length and separation angle.

	Re=20			Re=40		
Grid	75	100	150	75	100	150
θ_s	40.7119	41.3277	41.6750	50.7472	51.0249	51.5165
L	1.785711	1.773829	1.707539	4.301591	4.210746	4.041836

TABLE III. Comparison of geometric parameters with previous studies.

	Re	Reference [37]	Reference [38]	Reference [39]	Reference [40]	Reference [34]	Reference [35]	Reference [36]	Present
L	20	1.87	1.88	1.786	1.87	1.842	1.92	1.82	1.77
	40	4.65	4.69	4.357	4.27	4.49	4.51	4.48	4.21
C_D	20	2.0027	2.045	2.053	-	2.152	2.111	2.001	2.0597
	40	1.5359	1.522	1.550	-	1.499	1.574	1.498	1.5308
θ_s	20	-	43.7	-	-	42.96	42.79	42.9	41.3277
	40	-	53.8	-	-	52.84	52.84	51.5	51.0249

B. Initial and boundary conditions

The inviscid flow solution is taken as initial conditions and boundary conditions are imposed on the surface of the cylinder and also at far field which has been taken much away from the surface of the cylinder. In addition, the boundary conditions are also required at two symmetric lines when the problem is solved at low Reynolds numbers (Re <60) and on the artificial cut (the part of the domain on the negative x axis) when the problem is solved at intermediate and high Reynolds numbers. At low Reynolds numbers, the symmetric nature of the flow about the x axis has been exploited, and the solutions are obtained only on the upper part of the domain. In this case the symmetric boundary conditions have been used at the two symmetric lines taken on positive and negative sides of the x axis. However, for intermediate and high Reynolds numbers no symmetry of the flow has been used in the flow computations but periodic conditions have been imposed on the artificial cut (since the first and the last grid lines are one and the same in η direction) (refer to [32] for more details). At far field, both ψ and ω are known from the uniform flow conditions. Finally, on the surface of the cylinder, due to the no-slip condition, ψ becomes zero and the vorticity ω has been computed numerically using Briley's formula. To compute this, the fourth-order approximation of $\partial\psi/\partial\eta$ is obtained on the surface of the cylinder using one-sided (forward difference in this case) and central differences given by

$$\left(\frac{\partial\psi}{\partial\eta}\right)_{i,0} \approx \frac{-3\psi_{i,-1}-10\psi_{i,0}+18\psi_{i,1}-6\psi_{i,2}+\psi_{i,3}}{12h}, \tag{15}$$

$$\left(\frac{\partial\psi}{\partial\eta}\right)_{i,0} \approx \frac{\psi_{i,-2}-8\psi_{i,-1}+8\psi_{i,1}-\psi_{i,2}}{12h}, \tag{16}$$

where the negative subscripts represent ghost points outside the computational domain. From Eqs. (15) and (16) we have

$$\psi_{i,-1} = -\frac{10}{3}\psi_{i,0}+6\psi_{i,1}-2\psi_{i,2}+\frac{1}{3}\psi_{i,3}-4h\left(\frac{\partial\psi}{\partial\eta}\right)_{i,0}, \tag{17}$$

$$\psi_{i,-2} = -\frac{80}{3}\psi_{i,0}+40\psi_{i,1}-15\psi_{i,2}+\frac{8}{3}\psi_{i,3}-20h\left(\frac{\partial\psi}{\partial\eta}\right)_{i,0}. \tag{18}$$

To compute the vorticity on the surface of the cylinder, we use a fourth-order approximation of $\omega=-J^{-2}\gamma(\partial^2\psi/\partial\eta^2)$ which is equivalent to

$$\omega_{i,0} = -\frac{\gamma}{J^2}\frac{16(\psi_{i,-1}+\psi_{i,1})-(\psi_{i,-2}+\psi_{i,2})}{12h^2}. \tag{19}$$

Substituting Eqs. (17) and (18) into Eq. (19) and imposing the velocity component in the tangential direction as zero gives

$$\omega_{i,0} = -\frac{\gamma}{J^2}\left(\frac{108\psi_{i,1}-27\psi_{i,2}+4\psi_{i,3}}{18h^2}\right). \tag{20}$$

All the computations in the present investigation have been carried out using Eq. (20) as the boundary condition for vorticity on the surface of the cylinder. However, [33] has interpreted Jensen's formula, a formula similar to Eq. (20), as third-order accurate and also developed three different fourth-order formulas to approximate no-slip boundary conditions. After comparing the results of the lid driven cavity problem solved using various formulas, they have concluded that both Jensen's and higher-order Jensen's (HOJ) formulas have fair convergence and good accuracy, with HOJ giving slightly better approximations in most cases.

C. Numerical algorithm

1. Initialize ψ^n and ω^n.
2. Compute $\bar{\omega}^n$ using the Eq. (10).
3. Compute $\bar{\omega}^{n+1}$ using the Eq. (8).
4. Solve Eq. (7) for ψ^{n+1}.
5. Solve Eq. (10) for ω^{n+1}.
6. Repeat steps 3 to 5 until convergence.

Equation (8) is an ordinary differential equation of $\bar{\omega}$ with respect to the time t. The obvious choice to solve this equation is to use the fourth-order Runge-Kutta (R-K) method so that the time derivative also will be approximated to fourth order, however, this requires additional storage. Since the main interest in the present simulation is to show that the HOSC scheme can be used to solve complex flow problems in nonrectangular geometries, in the present investigation an explicit scheme (time derivative is approximated with forward difference approximation) has been incorporated for

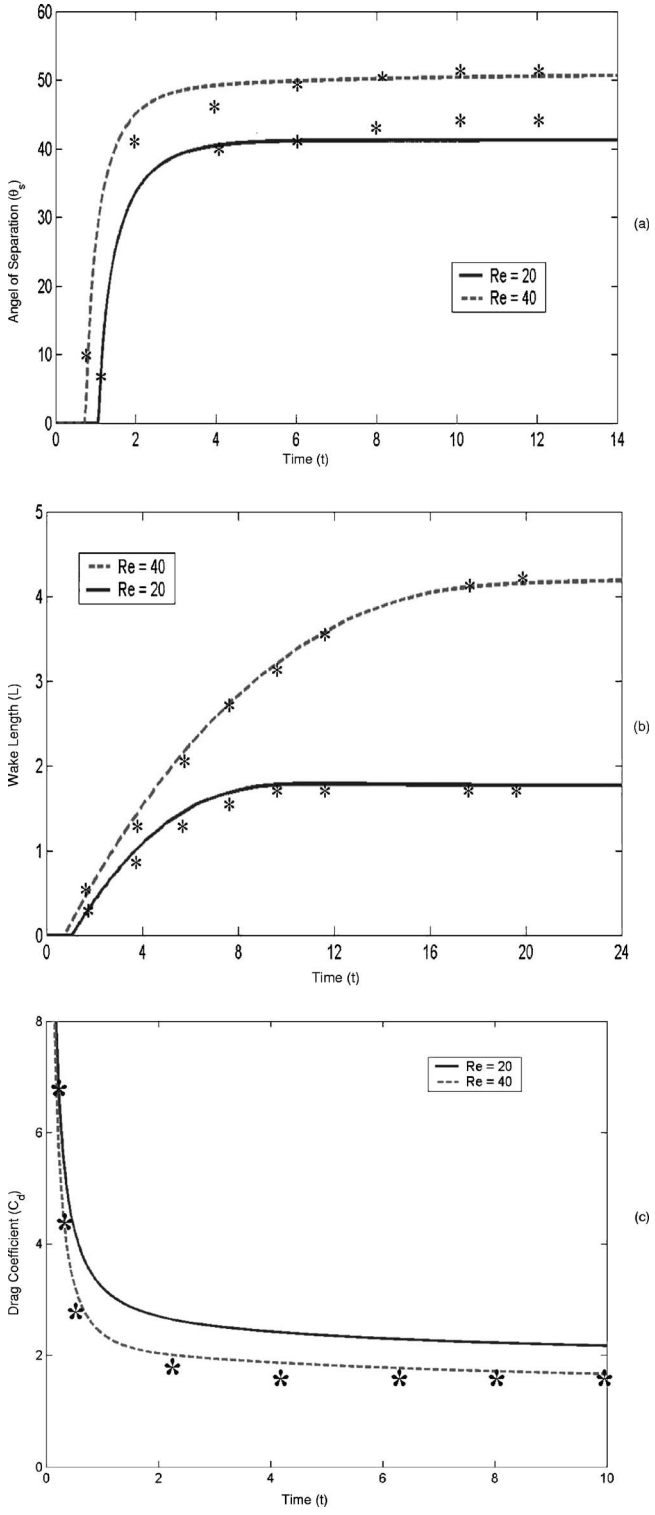

FIG. 3. Comparison of (a) angle of separation (Ref. [11]), (b) wake length (Ref. [11]) and (c) drag coefficient (Ref. [41]).

temporal approximation of Eq. (8). The computations are also carried out using the R-K Scheme however, there is no significant reduction in the CPU time is observed. Hence all the investigations are carried out using the explicit scheme. Similarly in steps 4 and 5, two elliptic equations have to be solved iteratively for ψ and ω. The equation in step 4 is an

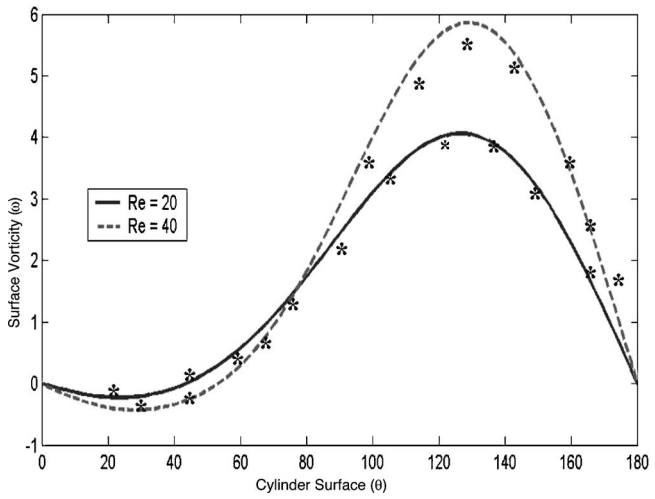

FIG. 4. Comparison of the vorticity on the cylinder (*-[36])

usual Poisons equation and the equation in step 5 is a strong diagonally dominant equation. Due to the diagonal dominant nature of these equations and also because of small time steps used in the computations, the successive over relaxation scheme, used for inner iterations, converged very quickly (<5 iterations). Instead of SOR scheme in computing ψ and ω in steps 4 and 5, we have also used Bi-conjugate gradient stabilized scheme. But this has increased the memory requirement without any significant reduction in the overall computational time. This may be due to the small step length used in the time direction.

IV. RESULTS AND DISCUSSION

The higher-order semicompact scheme briefly described in the earlier section has been used to simulate flow induced by an impulsively started circular cylinder. Initially, simulations at small Reynolds numbers were carried out to evaluate the accuracy of the present method. The obtained results have been compared qualitatively and quantitatively with previous experimental and numerical results. Then simulations at moderate and higher Reynolds numbers are used to demonstrate the ability of the present scheme in simulating the real flows.

A. Flows at Re=20 and 40

It is well known that the flows with Reynolds number less than 60, will eventually develop into a steady state. Therefore the results at these Reynolds numbers can be compared with the results of the corresponding steady state problem. The choice of Re=20 and 40 is due to the availability of experimental and numerical results at these Reynolds numbers. Only the upper half of the domain has been considered in the computations because it is again known that at these small Reynolds numbers the flow is symmetric about the x axis. Since the viscous effects are more close to the surface of the cylinder, a nonuniform distribution of grid points is used such that the grid density is much higher at the surface of the cylinder and reduces gradually to the outer boundary.

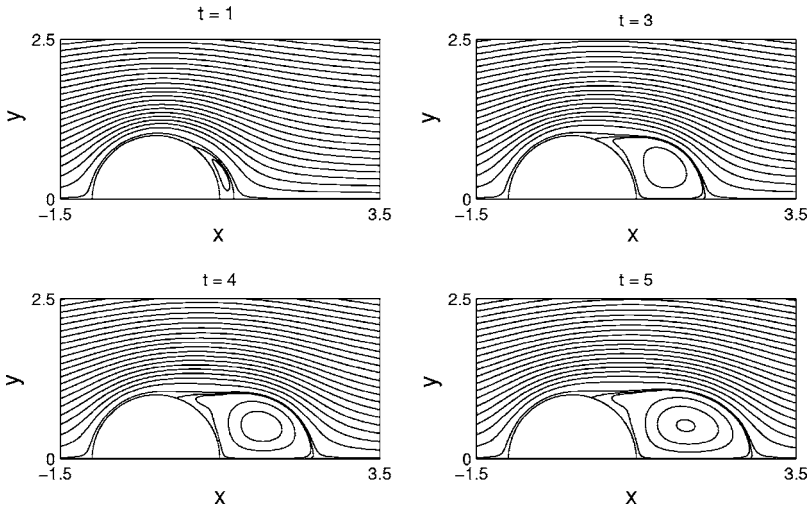

FIG. 5. Stream lines at Re=300.

The outer boundary in the form of a half circle is identified depending on the Re and the far field boundary conditions are applied. A typical computational mesh for flow at these Reynolds numbers around a half circular cylinder is given in Fig. 1. In this figure every alternate grid line has been given for an 100×100 size of the mesh.

The grid independence has been tested by varying the mesh sizes into $75\times75, 100\times100$, and 150×150. Also to test the dependence of far field boundary in O type grids the outer boundary is varied from 50 to 75 times the diameter of the cylinder. A time increment of 0.0005 is used in these computations.

Figure 2 gives the stream lines and vorticity lines when flow reaches its final steady state at Re=20 and 40. In both these cases stationary recirculating eddy develops behind the cylinder. The wake length L, the distance between the rear most point of the cylinder to the end of the wake, and the angle of separation θ_s are compared to verify the grid independence and dependence of far field boundary condition. In Table I these two geometric parameters have been compared by varying the far field boundary to 50.5, 62.5, and 75 times the diameter of the cylinder for Re=20 and 40. The mesh size has been fixed as 100×100 in these computations. It is clear from this comparison that a far field distance of 75 units gives reasonably accurate results. Similarly, in Table II the effect of grid densities has been given at Re=20 and 40. Here far field is fixed as 75 units.

Since the change of these geometrical parameters is very minimal for grid densities more than 100, the HOSC scheme can be taken as grid independent. The time is expressed as a/U units where a is the radius of the cylinder. Finally in Table III the wake length, angle of separation (θ_s) and Drag coefficient C_D are compared with various experimental and numerical results [34–40]. It is clear from Table III that, though some of the results of [34,35] deviate from the benchmark solution of [36] by more than 5%, the deviations of the present values varies from 0.9% to 6% with most of the variations centered at 2%. The good agreement of these geo-

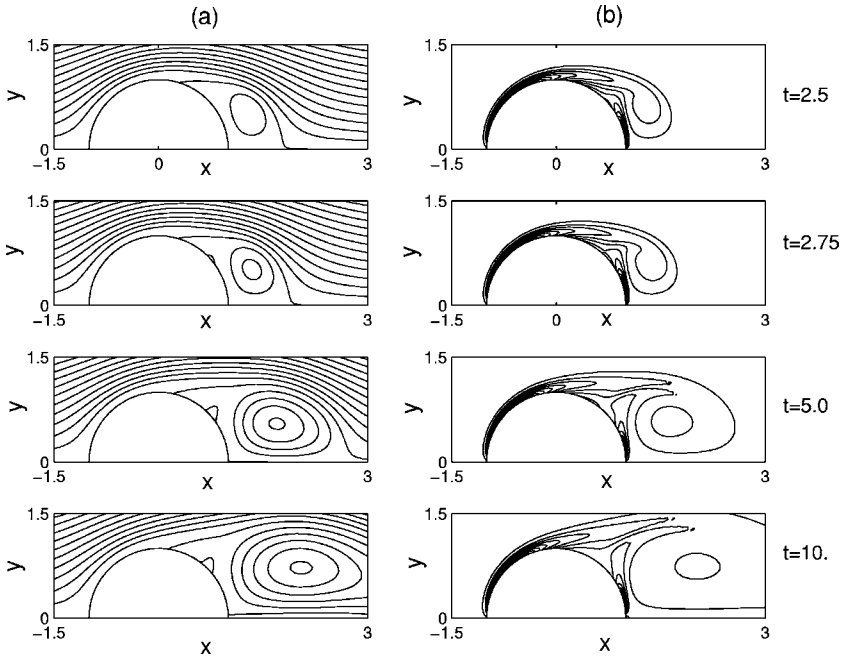

FIG. 6. (a) Stream lines and (b) vorticity lines at Re=550.

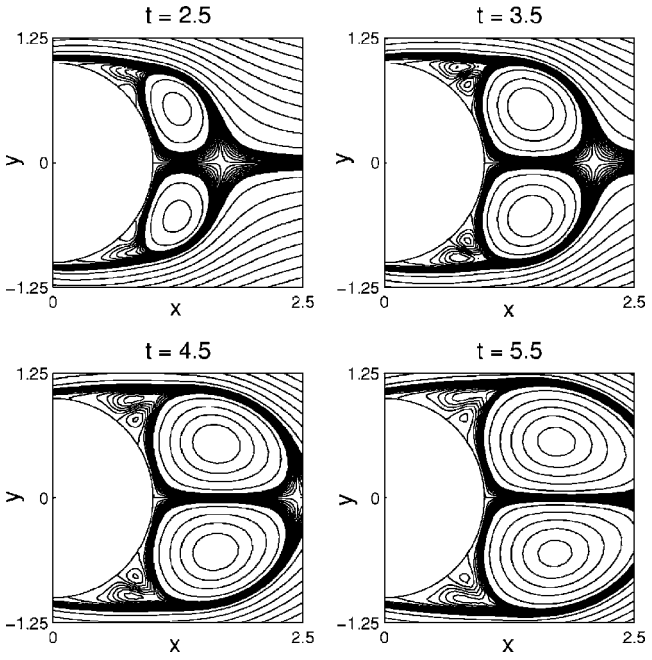

FIG. 7. Stream lines at Re=1000.

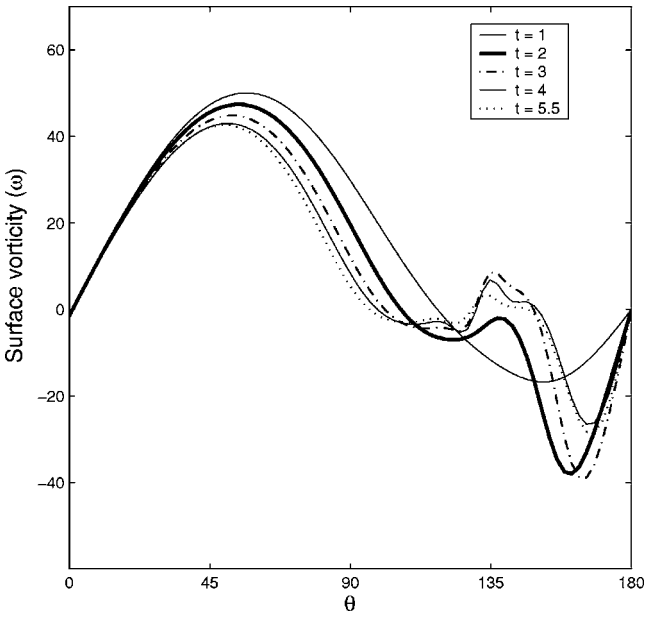

FIG. 8. Vorticity on the cylinder at Re=1000.

metric parameters with existing results confirms the performance of the HOSC scheme.

The drag coefficient C_D in Table III is computed from the integration of the pressure and shear forces around the cylinder using

$$C_D = \oint p y_\xi d\xi - \frac{2}{\mathrm{Re}} \oint \omega x_\xi d\xi, \tag{21}$$

where the surface pressure is defined by

$$p_2 - p_1 = \frac{2}{J\mathrm{Re}} \int_{\xi_1}^{\xi_2} (\beta\omega_\xi - \gamma\omega_\eta) d\xi. \tag{22}$$

In the actual computation of C_D, the first term of Eq. (21) is expanded using integration by parts and then $\partial p/\partial\xi$ from Eq. (22) is used to avoid the computation of pressure on the cylinder. To compare the evolution of separation angle, wake length, and drag coefficient with time at Reynolds numbers 20 and 40 the corresponding graphs are displayed in Fig. 3. In these comparisons the experimental results of [11,41] are also included. These comparisons clearly show that the results obtained by the present method agree well with the benchmark data. The vorticity distribution over the cylinder surface at the steady state, which has been computed numerically, is given in Fig. 4. The numerical results of [36] are included in this figure for the sake of comparison. Again a good agreement can be seen between the present and [36] results.

B. Flows at Re=300 and 550

After testing the developed code at small Reynolds numbers, the same has been used to simulate the flows at moderate Reynolds numbers. The flow around an impulsively started circular cylinder at these moderate Reynolds numbers is known to develop eventually into three-dimensional phenomenon. However, at the early stage of the development of the laminar wake region, the flow is still two dimensional and symmetric about the x axis. So the present study at these Reynolds numbers has been restricted to the early stage of the flow development. In this range of Re we have chosen the cases 300 and 550 because at these Re the experimental and numerical results are available and also reported the formation of a bulge and secondary eddy phenomena, respectively.

The flow patterns for Re=300 and Re=550 at different times have been given in Figs. 5 and 6, respectively. In this experiment the far field is fixed at 25 units and the size of the mesh is taken as 151×151. The time increment is fixed as 0.0001 in the whole computation. Figure 5 clearly shows the appearance of the bulge and increase of its size with time. However there is no formation of any secondary eddy even at the time $t=10$. As observed by [12] experimentally at $t=2.75$ and numerically by [40] at $t=2.85$ the present scheme, as shown in Fig. 6, also captures the formation of secondary vortex at time $t=2.75$ for Re=550. Using the lattice Boltzmann method [34] also captured the formation of this secondary vortex at time $t=2.75$. As shown in this figure, the size of the secondary vortex increases with time, however, it does not grow to touch the surface of the wake region even at time $t=10$. This is the feature again similar to what has been shown by [12,40–42]. To validate the concentration of vorticity in the vicinity of the cylinder, the equivorticity lines have been also shown in Fig 6. These patterns are also in close agreement with the existing literature. All the computations at these Re have been done with and without using symmetry of the flow to verify the accuracy of the computations.

C. Flows at Re=1000 and 5000

The choice of Re=1000 is to demonstrate the capability of the present scheme in capturing the α phenomenon. It is

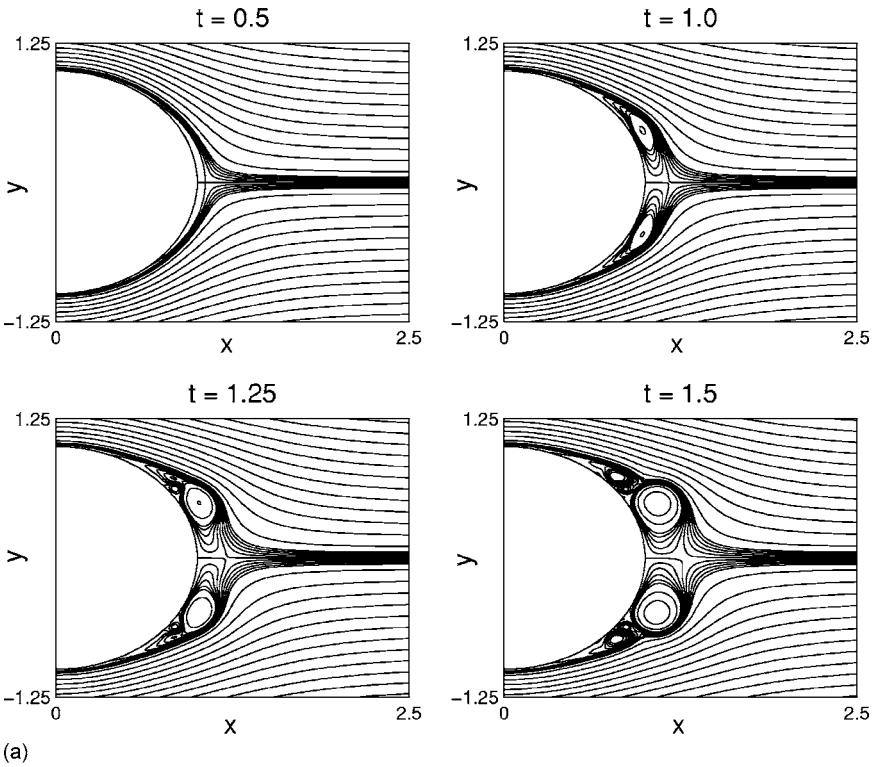

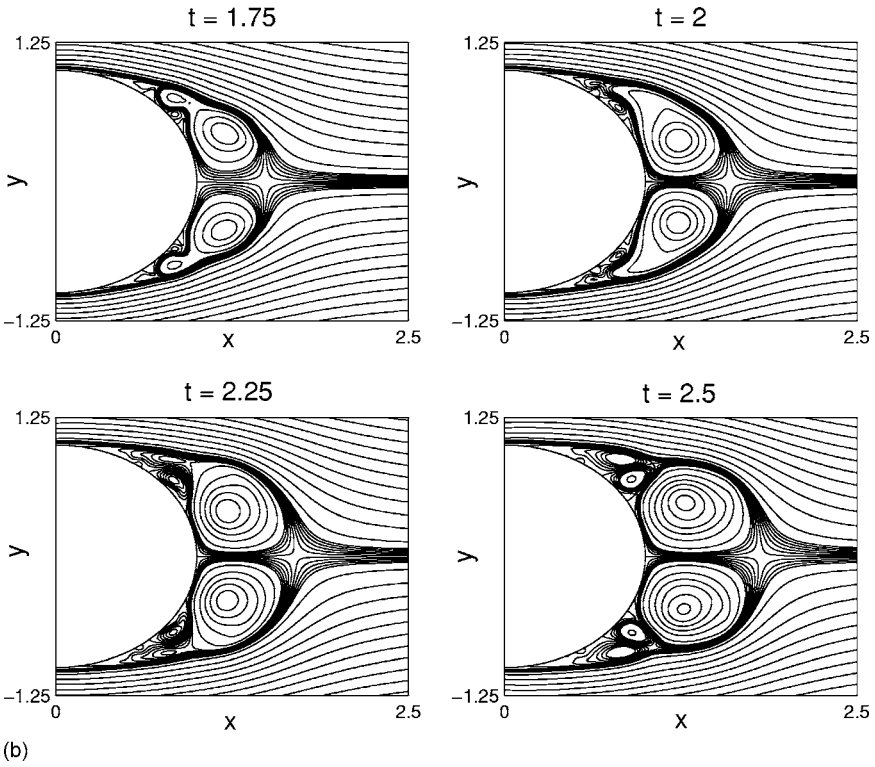

FIG. 9. (a) Formation of β phenomenon at Re=5000 and (b) formation of α phenomenon at Re=5000.

known from the experimental results of [11] that for the flows at Reynolds numbers between 800 and 5000 there is a formation of α phenomenon. At times t around 1.5 when the main eddy is still stable, the secondary eddy develops enough in size for its exterior boundary to touch the boundary of the main recirculating zone thus splitting the main eddy into two parts and isolating the region of the wake next to the separation point in which another secondary eddy is formed. These two secondary eddies thus formed are equivalent in size and in strength and constitute "a pair of secondary eddies." This particular formation of the streamline structure is named as α phenomenon by [12]. They have also observed the formation of β phenomenon at Reynolds number 5000 and above. At these Reynolds numbers, at the very

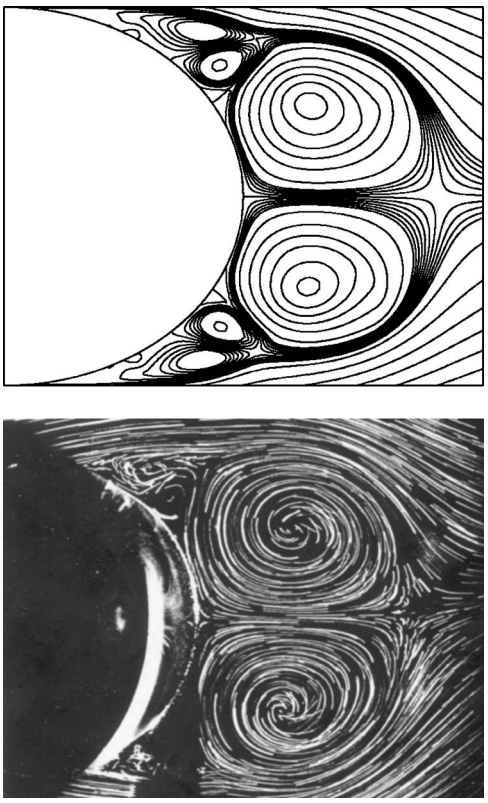

FIG. 10. Comparison of flow patterns for Re=5000 at time $t=2.5$ (a) present results, (b) (Ref. [12]).

early phase of the flow establishment, a very thin recirculating wake (fitting exactly the cylinder shape) is formed. However, very soon at $t=0.75$ next to the cylinder wall, the core of this recirculating zone (which seems to correspond to a vorticity peak) rotates in one piece, very quickly in comparison with the velocities in the other part of the separated zone, and is individualized in a "vortex" that is increasing with time in size and strength. Then at time $t=1$, particular vortex separates the initial wake into two parts. The one situated near the separated point S is occupied by a pair of secondary eddies whose structure is roughly similar to those described before but which however differ in details. The second part remains more or less in communication with the rapid rotating vortex. For $t=1.25$ it is seen that the vortex progressively replaces the initial wake "absorbing" the zones on either side, including the one occupied by the pair of secondary eddies. At $t=1.5$, the initial wake, which [11] has called as the "forewake," has practically vanished and the "mainwake" is formed. Since this phenomenon can be observed for Re greater than or equal to 5000, we have chosen Re=5000, so that we can demonstrate the formation of both β and α phenomena one after the other.

For Re=1000, the far field is fixed at 12 times the diameter of the cylinder and a 201×201 grid has been used. The streamline contours are shown in Fig. 7. In this figure the flow patterns at time $t=2.5$, 3.5, 4.5, and 5.5 are given to show the appearance of secondary eddy and splitting of the main eddy into two parts, isolating the region of the wake next to the separation point, wherein a second secondary eddy is formed. These flow structures again compare well

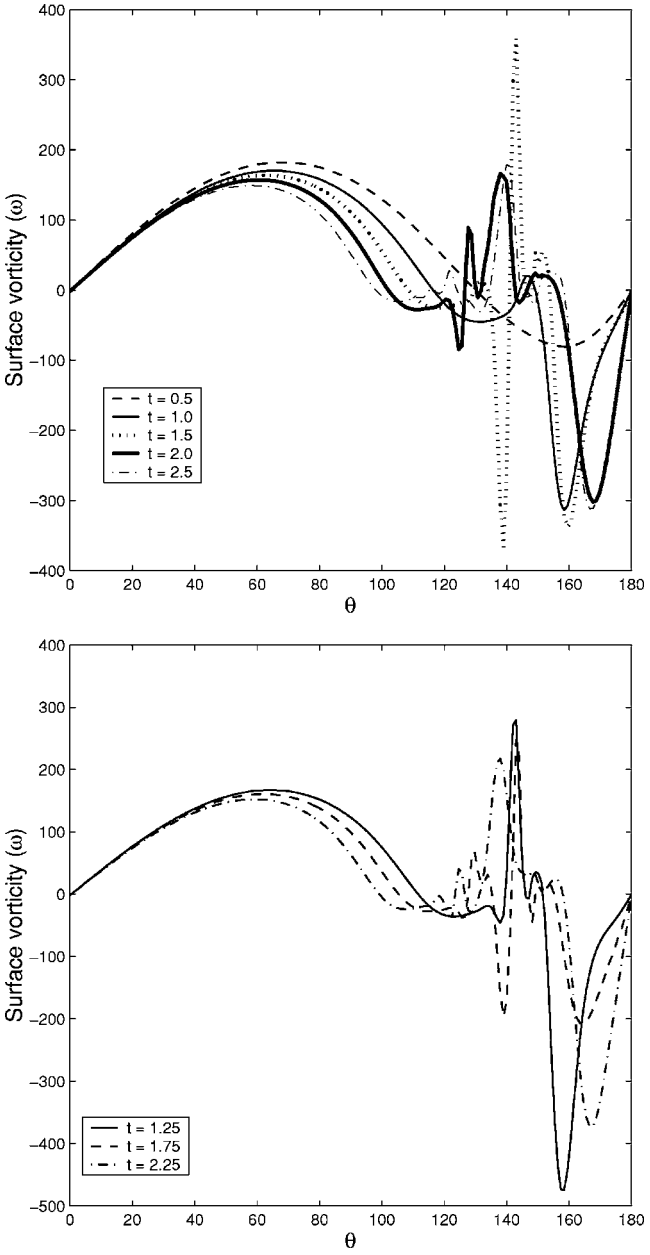

FIG. 11. Vorticity on the cylinder at Re=5000.

with the experimental illustrations of [11]. The vorticity distribution over the cylinder surface for Re=1000 at various times is given in Fig. 8.

Figures 9(a) and 9(b) give the time evolution streamline patterns at Re=5000. These computations have been performed on a 351×351 grid with outer boundary fixed at ten times the diameter of the cylinder. The time increment is again fixed as 0.0001. Figure 9(a) clearly shows the formation of β phenomenon at $t=1.5$ however, the isolated part of the vortex again coalesce with other parts of the wake region, as shown in Fig. 9(b), and forms the α phenomenon at time $t=2.5$. This phenomenon simulated using the HOSC scheme has been compared with the only available experimental results of [12] in Fig. 10. The vorticity on the surface of the cylinder for Re=5000 at various times is given in Fig. 11.

V. CONCLUSIONS

The classical problem of unsteady viscous incompressible flow past an impulsively started circular cylinder has been solved using higher-order semicompact scheme. The separated flows behind the circular cylinder have been simulated until steady state for low Reynolds numbers and during the early stages of the flow for moderate and high Reynolds numbers. The results obtained have been compared and found in good agreement with existing experimental and computational results. The geometric parameters like flow separation and length of the wake have been also compared with previous results and found satisfactory. The main advantage of the HOSC scheme is its applicability to arbitrary irregular domains with a nonuniform compact stencil. To avoid too much algebraic manipulation which is necessary for conventional compact schemes, in this scheme the compactness has been relaxed for a few terms in the higher-order approximation. Exploiting these advantages of the HOSC scheme we have captured the appearance of α phenomenon at Re=1000 and both β and α phenomena one after the other at times 1.5 and 2.5, respectively for Re=5000.

[1] H. Blasius, Z. Angew. Math. Phys. **56**, 1 (1908).
[2] S. Goldstein and O. C. Rosenhead, Proc. Am. Philos. Soc. **32**, 392 (1936).
[3] H. Schuh, Z. Flugwiss. **1**, 122 (1953).
[4] H. Wundt, Ing.-Arch. **23**, 212 (1955).
[5] E. J. Watson, Proc. R. Soc. London, Ser. A **231**, 104 (1955).
[6] C. Y. Wang, J. Math. Phys. **46**, 195 (1967).
[7] W. M. Collins and S. C. R. Dennis, Q. J. Mech. Appl. Math. **26**, 53 (1973a).
[8] M. Bar-lev and H. T. Yang, J. Fluid Mech. **72**, 625 (1975).
[9] H. Honji and S. Taneda, J. Phys. Soc. Jpn. **27**, 1668 (1969).
[10] S. Taneda, *Recent research on unsteady boundary layers*, Vol. 2 (Laval University, Quebec, 1972), p. 1165.
[11] M. Coutanceau and R. Bouard, J. Fluid Mech. **79**, 231 (1977); **79**, 257 (1977).
[12] R. Bouard and M. Coutanceau, J. Fluid Mech. **101**, 583 (1980).
[13] R. B. Payne, J. Fluid Mech. **4**, 81 (1958).
[14] D. B. Ingham, J. Fluid Mech. **31**, 815 (1968).
[15] M. Kawaguti and P. C. Jain, J. Phys. Soc. Jpn. **21**, 2055 (1966).
[16] J. S. Son and T. J. Hanratty, J. Fluid Mech. **35**, 369 (1969).
[17] P. C. Jain and K. Sankara Rao, Phys. Fluids **12**, Suppl. II, 57 (1969).
[18] S. C. R. Dennis and A. N. Staniforth, Lect. Notes Phys. **8**, 343 (1971).
[19] W. M. Collins and S. C. R. Dennis, J. Fluid Mech. **60**, 105 (1973b).
[20] S. C. R. Dennis and J. D. Hudson, J. Comput. Phys. **85**, 390 (1989).
[21] M. M. Gupta, J. Comput. Phys. **93**, 343 (1991).
[22] M. Li, T. Tang, and B. Fornberg, Int. J. Numer. Methods Fluids **20**, 1137 (1995).
[23] W. F. Spotz and G. F. Carey, Int. J. Numer. Methods Eng. **38**, 3497 (1995).
[24] B. J. Noye, Commun. Appl. Numer. Methods **6**(4), 279 (1990); **7**(7), 501 (1991).
[25] S. Abarbanel and A. Kumar, J. Sci. Comput. **3**, 275 (1988).
[26] W. F. Spotz and G. F. Carey, Numer. Methods Partial Differ. Equ. **17**, 657 (2001).
[27] E. Weinan and J. G. Liu, J. Comput. Phys. **126**, 122 (1996).
[28] Y. V. S. S. Sanyasiraju and V. Manjula, Comput. Mech., **35**, 441 (2005).
[29] S. R. K. Iyengar and R. Manohar, J. Comput. Phys. **77**, 425 (1988).
[30] M. K. Jain, R. K. Jain, and M. Krishna, Commun. Numer. Methods Eng. **10**, 791 (1994).
[31] M. C. Lai, J. Comput. Phys. **182**, 337 (2002).
[32] J. F. Thompson, Z. U. A. Warsi, and C. W. Mastin, *Numerical Grid Generation-Foundation and Applications* (North-Holland, Amsterdam, 1985).
[33] W. F. Spotz, Int. J. Numer. Methods Fluids **28**, 737 (1998).
[34] X. He and G. Doolen, J. Comput. Phys. **134**, 306 (1997).
[35] X. D. Niu, Y. T. Chew, and C. Shu, J. Comput. Phys. **188**, 176 (2003).
[36] B. Fornberg, J. Fluid Mech. **98**, 819 (1980).
[37] H. Takami and H. B. Keller, Phys. Fluids **12**, Suppl. II, 51 (1969).
[38] S. C. R. Dennis and G. Z. Chang, J. Fluid Mech. **42**, 471 (1970).
[39] F. Nieuwstadt and H. B. Keller, Comput. Fluids **1**, 59 (1973).
[40] T. P. Loc, J. Fluid Mech. **100**, 111 (1980).
[41] P. K. Koumoutsakos and A. Leonard, J. Fluid Mech. **296**, 1 (1995).
[42] C. C. Chang and R. L. Chern, J. Fluid Mech. **233**, 243 (1991).